High-resolution vibrational spectroscopy of Pb-OH defects in $KMgF_3$ fluoroperovskite single crystals

A. Baraldi, P. Bertoli, R. Capelletti, and A. Ruffini*
Istituto Nazionale per la Fisica della Materia (INFM), Physics Department, University of Parma, Parco Area delle Scienze 7A, 43100 Parma, Italy

A. Scacco
Istituto Nazionale per la Fisica della Materia (INFM), Physics Department, University of Rome ''La Sapienza,'' Piazzale A. Moro 2, 00185 Rome, Italy

(Received 19 September 2000; published 13 March 2001)

High-resolution (0.04 cm^{-1}) Fourier transform infrared spectroscopy in the temperature range 9–300 K is applied to detect and analyze the OH^- stretching modes in air grown $KMgF_3$ single crystals, doped with different Pb amounts. In addition to the 3733.7 cm^{-1} line attributed to the stretching mode of isolated OH^-, two main lines peaking at 3550.9 and 3567.7 cm^{-1} are due to the OH^- stretching modes perturbed by neighboring Pb defects. Suitable thermal treatments and isotopic substitutions provide models of the complexes in which OH and Pb are embedded. Lead is recognized as favoring the OH^- inclusion into the lattice and causing an inhomogeneous broadening of the IR lines related to the stretching modes of OH^- interacting with other cation impurities. Anharmonicity effects are monitored by the weak overtones of the OH-related lines and discussed in the framework of the Morse model for the anharmonic oscillator. The anharmonicity and the Morse parameters, which show a very weak temperature dependence in the 9–300 K range, are very close to those displayed by alkali fluorides. The temperature dependence of the line position and linewidth of the narrow (0.4–0.9 cm^{-1}) Lorentzian-shaped IR lines and of the related overtones is successfully analyzed by means of the single phonon coupling model. The coupled phonon frequencies, evaluated from the fitting, for the Pb-perturbed OH^- stretching modes fall in the frequency range of the highest phonon state density of the host matrix.

DOI: 10.1103/PhysRevB.63.134302 PACS number(s): 78.30.−j, 63.20.Pw, 63.20.Mt, 71.55.−i

I. INTRODUCTION

Perovskites are a wide class of materials, the general formula being ABX_3 (A and B are cations and X an anion), which have recently attracted considerable interest owing to the discovery of high-T_c superconductivity and colossal magnetoresistance. Among the insulating perovskites, many ABO_3 and ABF_3 compounds are also attractive for technological applications. Ferroelectricity, piezoelectricity, and large nonlinear optical and electro-optical coefficients are features exhibited by some compounds of the former family, the most widely studied and exploited being $LiNbO_3$.

Fluoroperovskites, described by the formula ABF_3 (A being an alkali ion and B an alkaline-earth or a transition-metal divalent ion) also exhibit interesting technological applications. To be more precise, the cubic $KMgF_3$, if properly doped, can be exploited as a host medium for lasing centers,[1,2] thermoluminescent dosimeters,[3,4] and scintillators.[5–7] In this framework great interest has been devoted to the study of defects (either due to impurities or induced by radiation damage) which show a radiative decay from the excited states. $KMgF_3$ single crystals doped with different classes of cation impurities, such as rare earths (Ce, Eu, Sm, Tb),[3,8–10] transition metals (V, Cr, Mn, Fe, Co, Ni),[1,11–16] metal-ions with the $(nd)^{10}$ and $(ns)^2$ electronic configurations (Ag^+, Cu^+; and Tl^+, Pb^{2+}, respectively),[2,17–21] have been widely investigated by a variety of techniques, such as emission and absorption spectroscopies,[1–3,8–10,12,13,17–20] optically detected magnetic resonance (ODMR),[21] and electron nuclear double resonance (ENDOR),[16] and have been described by theoretical models.[11,13–15]

However, the literature relating to defects induced by anion impurities in fluoroperovskites is rather poor, although, as an example, the presence of oxygen as unwanted dopant is expected and detected.[22] Among anion impurities, hydroxyl ion deserves particular attention since it enters the matrix during the crystal growth from the melt, especially if this is performed in air.[23,24] It interacts easily with other impurities, e.g., cations, giving rise to complexes which deeply modify the particular impurity-induced properties, as is well known in alkali halides.[25] In crystals and glasses, this type of interaction causes the undesirable quenching of the luminescence due to rare earths,[26] and, as a consequence, should be carefully avoided. In contrast, in perovskitic oxides, the hydrogen related defects, and among them OH,[27,28] favorably affect various physical properties which can be exploited for device applications: examples are the reduced laser optical damage and the thermal fixing of the volume holograms in $LiNbO_3$ single crystals.[29] Moreover, several perovskite-structured oxides become good high-temperature protonic conductors after protons are introduced, as a consequence of the OH doping.[30] The presence of OH in $KMgF_3$ crystals has been detected by means of the broad UV absorption band peaking at 187 nm and attributed to the electronic transition of the OH^- centers.[22] However, the UV peak, as in alkali halides, accounts for all the OH-related defects, being unable

to discriminate among different environments in which OH might be embedded, as a consequence of its interaction with other impurities. Such a fine analysis can be successfully pursued by monitoring the OH^- stretching absorption, a very sensitive probe of slightly different surroundings, as proved by the high-resolution infrared (IR) spectroscopy, applied at low temperatures to alkali halides and sillenites,[25,31,32] and, more recently, in a preliminary way to $KMgF_3$.[33]

In the present work high-resolution (0.04 cm^{-1}) Fourier transform infrared (FTIR) spectroscopy in the temperature range 9–300 K is exploited to detect the OH^- stretching modes in $KMgF_3$ single crystals and to monitor their interaction mainly with Pb, which has been proved to be a lasing impurity.[2] Suitable thermal treatments are applied in order to identify the nature and supply models of the complexes in which OH and Pb are embedded. Possible anharmonicity effects are investigated by analyzing the isotopic replica and the weak overtones of the OH-related spectra and are discussed in the framework of the Morse model for the anharmonic oscillator. The anharmonicity and the Morse parameters are compared to those of OH-stretching modes in materials of similar crystalline structure, such as the perovskitic oxides, and in alkali fluorides, which have a similar ionic character. The careful analysis of the line shape, position and line width of the narrow IR lines, as a function of the temperature, is exploited to provide a model for the OH-stretching mode coupling to the lattice vibrations. The coupled phonon frequencies, evaluated by using the single phonon-coupling model,[34] are compared to those of the host matrix.

II. EXPERIMENTAL DETAILS

$KMgF_3$ single crystals were grown by means of the Czochralski method. The starting powders were a mixture of dried and precrystallized KF and MgF_2 reagent grade materials mixed in the stoichiometric ratio. The Pb doped crystals were obtained by adding to the above mixture the desired amount of $PbBr_2$ or PbF_2, in a mole fraction ranging between 0.5 and 5%. For comparison, a few crystals doped with AgI, in a mole fraction ranging between 2.5 and 12.5 %, were also prepared. Most of the crystals were grown in air in order to introduce OH^-, but some of them were grown in Ar atmosphere and OH^- was added as alkali hydroxide, e.g., KOH or NaOH, in a mole fraction ranging between 1 and 2 %. The isotopic substitution of OD for OH was obtained by keeping the crystal at 950 °C (a temperature close to the $KMgF_3$ melting point, i.e., 1050 °C) in dry nitrogen bubbling through D_2O for about one hour. The samples submitted to the above treatment exhibited a milky surface layer which largely contributed to the light scattering [as an example, see Fig. 3, curves (e) and (f)]. Thermal treatments, such as quenching and annealing from 650 °C, were performed in air.

The IR absorption spectra were acquired by means of an FTIR Bomem DA8 spectrophotometer with an apodized resolution as good as 0.04 cm^{-1} in the range 600–7500 cm^{-1}. The ultraviolet-visible (UV-vis) absorption spectra were measured at the Adone storage ring of the Laboratori Nazionali di Frascati in the range 4–12.5 eV and by means of a Varian 2390 dispersive spectrophotometer in the range 1.5–6 eV. The IR spectra were monitored in the temperature range 9–300 K by assembling the sample in a 21SC model Cryodine Cryocooler from CTI Cryogenics.

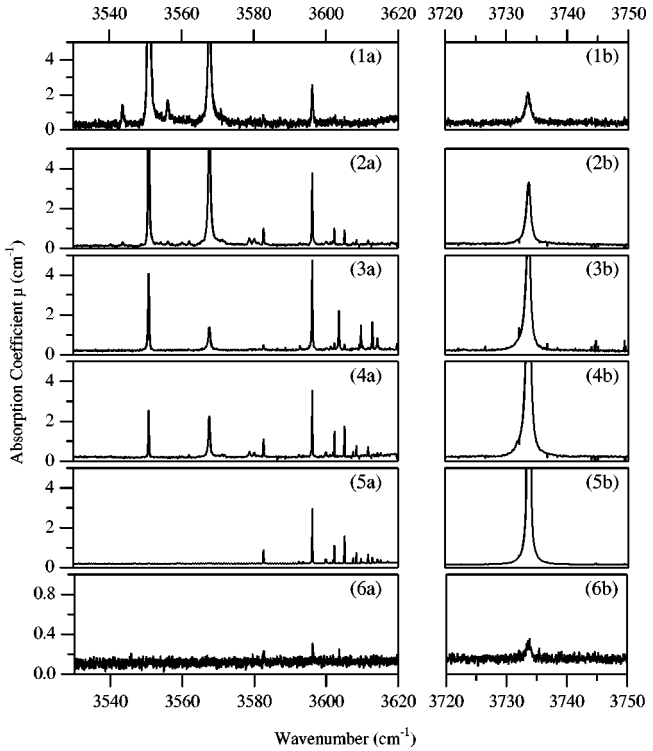

FIG. 1. High resolution (0.04 cm^{-1}) IR absorption spectra measured at 9 K of $KMgF_3$ samples (in the following the sample number is enclosed in brackets) nominally doped with different impurities (the amount added to the melt is expressed in molar fractions, m.f.). Curves (1): 5% $PbBr_2$ (K7); curves (2): 0.5% $PbBr_2$ (K3); curves (3): 0.5% $PbBr_2$ (K4); curves (4): 2.5% AgI (K0); curves (5): 12.5% AgI (K14); curves (6): 1% KOH (K6). The first five samples were grown in air, while the last was grown in inert Ar atmosphere. Left: spectra in the region of impurity perturbed OH^- stretching modes. Right: line due to the isolated OH^- stretching mode.

III. EXPERIMENTAL RESULTS

Figure 1 summarizes the IR spectra measured at 9 K in the 3530–3620 cm^{-1} range (column on the left) and in the 3720–3750 cm^{-1} range (column on the right) for $KMgF_3$ samples where Pb is present, to a greater or lesser extent, either because it is intentionally added to the melt (see Sec. II) or as an unwanted impurity. The Pb concentration decreases from the top to the bottom in Fig. 1, as monitored by the UV absorption band peaking at 248 nm (Ref. 20) (see below and Fig. 2). Many narrow lines are displayed by the spectra of the air grown samples [see curves (1)–(5) in Fig. 1], while they are fewer and weaker in samples grown in inert atmosphere (Ar), notwithstanding the addition of KOH to the melt [see curves (6) in Fig. 1]. The wave number range in which the narrow lines are detected is typical for the OH^--stretching mode absorptions in alkali halides.[23,24,31]

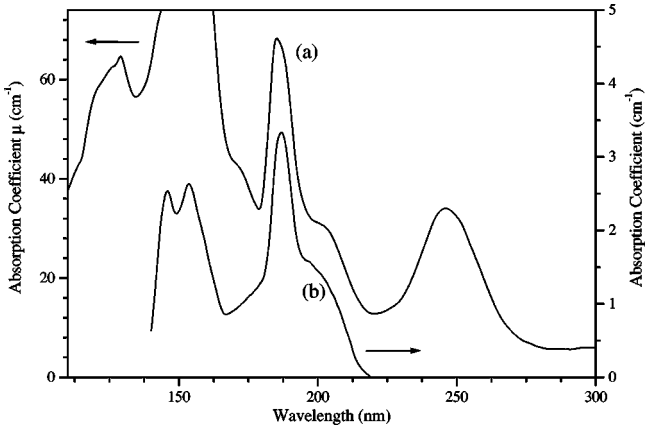

FIG. 2. VUV absorption spectra measured at 300 K of $KMgF_3$ samples nominally doped with Pb and OH. Curve (a): $KMgF_3$ doped with 0.5% $PbBr_2$ m.f. and grown in air (scale on the left); curve (b): $KMgF_3$ doped with 1% KOH m.f. and grown in inert Ar atmosphere (scale on the right).

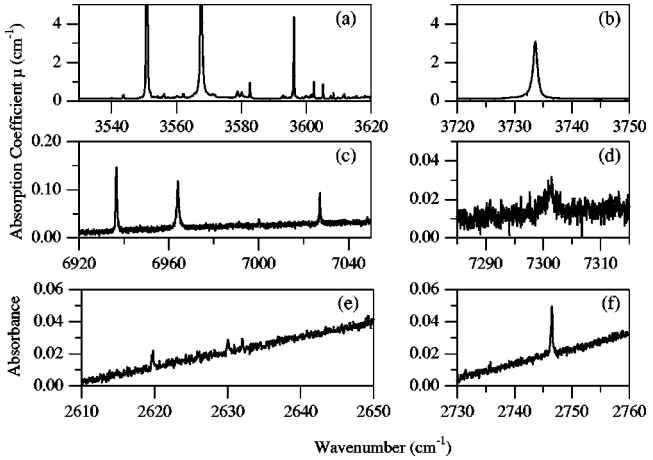

FIG. 3. High-resolution (0.04 cm^{-1}) IR absorption spectra measured at 9 K of $KMgF_3$ samples doped with 0.5% PbF_2 m.f. and grown in air (K21). Curves (a) and (b) are related to the fundamental transitions ($\Delta n=1$); curves (c) and (d) to the overtone transitions ($\Delta n=2$); curves (e) and (f) to the fundamental transitions ($\Delta n=1$) of a sample submitted to the deuteration process. Left: spectra in the region of impurity perturbed hydroxyl ion stretching modes. Right: line due to the isolated hydroxil ion stretching mode.

The OH^- doping is proved by the broad UV absorption band peaking at 187 nm and attributed to the electronic transition in OH centers[22] (see Fig. 2). This absorption is strong in samples grown in air and Pb doped [see curve (a), scale on the left], but much weaker in those to which only KOH has been added to the melt [see curve (b), scale on the right].

As for alkali halides codoped with OH^- and divalent cation impurities,[25] two regions can be distinguished in the OH^--stretching mode spectra of $KMgF_3$ (see Fig. 1). The former, at high wave numbers (see right side column spectra), is characterized by a line peaking at 3733.7 cm^{-1} common to all samples, independently of the codoping cation (e.g., Pb, Ag, Cu, etc.[33,35]): the line is attributed to OH not interacting with any impurity (isolated OH^-), see Sec. IV A. The latter, at shorter wave numbers (see left side column spectra), involves lines which are detected only if codoping cations are present. Their positions depend on the specific cation: these lines are attributed to OH^- perturbed by a neighboring cation impurity. In the present case the lines peaking at 3550.92 and 3567.72 cm^{-1} are ascribed to OH^- interacting with a Pb-induced defect (see Sec. IV A), and those peaking at 3596.2 and 3582.7 cm^{-1} to OH^- interacting with Cu.[35]

To support the attribution of the lines displayed in Fig. 1 to OH^--induced defects, the isotopic substitution of OD for OH was performed (see Sec. II). As a consequence, the 3733.7 cm^{-1} line shifts to 2747.5 cm^{-1} [see Fig. 3 curve (f) and Table I] and the two lines peaking at 3550.92 and 3567.72 cm^{-1} shift to 2619.7 and 2630.1 cm^{-1}, respectively [see Fig. 3 curve (e) and Table I], according to the relation

$$\frac{\Delta G_{10}^{\mathrm{OH}}}{\Delta G_{10}^{\mathrm{OD}}}=\sqrt{\frac{\mu_{\mathrm{OD}}}{\mu_{\mathrm{OH}}}}, \tag{1}$$

where ΔG^{OH} and ΔG^{OD} are the absorption line wave numbers in the hydroxylated and deuterated samples respectively, and μ_{OD} and μ_{OH} are the reduced masses of the free OH and OD diatomic molecules, respectively. Moreover, very weak replicas of the main lines peaking at 3733.7, 3567.72, and 3550.9 cm^{-1} appear at wave numbers by ≈ 11 cm^{-1} lower, as indicated by arrows in Fig. 4. The shift is accounted for by Eq. (1), if, in the hydroxyl group ^{16}O is replaced by ^{18}O (instead of H by D), and is in agreement with that observed for the free hydroxyl radical.[36] Thanks to the sensitivity of high-resolution FTIR spectroscopy applied at 9 K, the ^{18}O replicas were observed in hydroxylated samples, as a consequence, not of an intentional substitution of ^{18}O for ^{16}O, but simply of its natural abundance, which is as low as 2×10^{-3}. In alkali halides the same shift was detected for similar weak replicas, whose amplitude considerably increased in ^{18}OH-enriched samples, supporting the above attribution[32] (see Table I).

The fulfillment of Eq. (1) within 2% suggests that anharmonicity effects might occur. The hypothesis was confirmed by the weak overtones detected at wave numbers roughly twice those at which the main lines are monitored: compare curves (c) and (d) with curves (a) and (b), respectively, in Fig. 3. For this purpose, thick and/or heavily doped samples were particularly suitable.

Table I displays the position and width (as measured at 9 K) of the main lines monitored either in hydroxylated or deuterated samples and of their overtones. By increasing the sample temperature from 9 to 300 K, the lines become increasingly weaker, broadening and shifting (see Fig. 5), as a consequence of both the phonon coupling of the OH^--vibrational modes and the lattice thermal expansion (see Sec. IV D). An example is supplied by Fig. 5, where two spectra measured at 300 K (top) and at 9 K (bottom) are compared: many lines can be detected only at low temperatures.

In order to obtain information as to possible association and dissociation processes between hydroxyl ions and cation impurities (lead in the present case), Pb-doped samples,

TABLE I. Stretching-mode parameters for isolated hydroxyl and hydroxyl-perturbed by impurity defects in $KMgF_3$ and in a few different matrices or species. The line positions ΔG_{10}, ΔG_{20} and linewidths Γ_{10} and Γ_{20}, measured at 9 K, are related to $\Delta n=1$ and $\Delta n=2$ transitions, respectively. Different isotopic substitutions within the hydroxyl ion are indicated in the column headings. The linewidth figures for isolated OH^- and Cu-OH^- defects in $KMgF_3$ are related to ''Pb-free'' samples (see Sec. IV B).

Matrix or species	Impurity	ΔG_{10} (^{16}OH) cm^{-1}	Γ_{10} (^{16}OH) cm^{-1}	ΔG_{10} (^{18}OH) cm^{-1}	ΔG_{10} (^{16}OD) cm^{-1}	ΔG_{20} (^{16}OH) cm^{-1}	Γ_{20} (^{16}OH) cm^{-1}
$KMgF_3$	Pb	3543.68	0.30				
	Pb	3550.92	0.22	3540.3	2619.7	6936.7	0.6
	Pb	3556.29	0.43				
	Pb	3562.11	0.30				
	Pb	3567.72	0.60	3557.4	2630.1	6963.7	1.0
	Pb	3578.77	0.58				
	Pb	3580.13	0.75				
	Cu	3582.73	0.15		2642.2	7000.2	0.6
	Cu	3596.20	0.14		2651.6	7027.1	0.5
		3733.69	0.83	3722.7	2746.5	7301.3	2.0
LiF	Mg	3573.6[a]	0.13[a]	3562.6[a]	2637.5[a]	6977.9[a]	
		3735.4[a]	5.7[b]	3723.9[a]	2747.9[a]		
NaF	Mg	3592.5[a]	0.23[a]	3581.3[a]	2650.5[a]	7018.0[a]	
		3737.4[a]	$\leqslant 1.3$[b]		2747.8	7300.8[b]	3.6[b]
free OH^-		3555.606[c]		3544.455[c]			

[a]From Ref. 32.
[b]From Ref. 31.
[c]From Ref. 36.

grown in air, were submitted to appropriate thermal treatments, such as quenching and annealing. Figure 6 compares the spectra measured at 9 K of as grown sample [curves (1a) and (1b)], of the same sample quenched, i.e., rapidly cooled from 650 °C [curves (2a) and (2b)], and annealed, i.e., slowly cooled from the same temperature [curves (3a) and (3b)]. The quenching procedure causes a decrease of the lines due to OH^--vibrational modes perturbed by Pb and an increase of that related to the isolated OH^- [compare curves (1a) and (1b) with curves (2a) and (2b), respectively], in Fig. 6, while the annealing induces a partial recovery of the initial spectrum [compare curves (1a) and (1b) with curves (3a) and (3b), respectively].

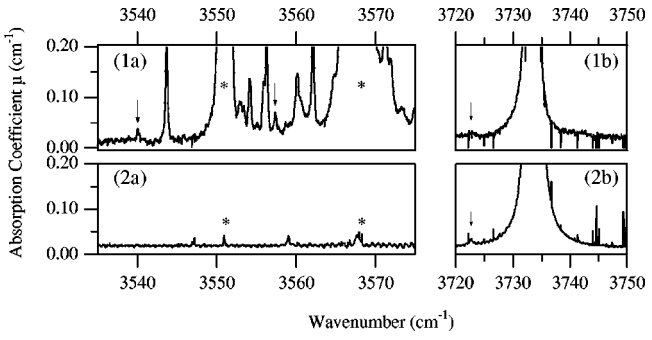

FIG. 4. High-resolution (0.04 cm^{-1}) IR absorption spectra measured at 9 K of $KMgF_3$ samples to show the isotopic replicas of the main ^{16}OH-modes due to ^{18}O present in natural abundance as low as 2×10^{-3}. The weak isotopic replicas are indicated by arrows and fall at ≈ 11 cm^{-1} below the related main bands (out of scale, for the sake of clarity). Curves (1): $KMgF_3$ doped with 0.5% PbF_2 m.f. (K21); curves (2): $KMgF_3$ doped with 12.5% AgI m.f. (K14). Both samples were grown in air. The stars over curve (2a) indicate the lines due to weak Pb traces in a nominally Pb-free sample [compare their positions with those of the main bands in curve (1a), due to Pb-OH defects]. Left: spectra in the region of impurity perturbed OH^- stretching modes. Right: lines due to isolated OH^- stretching modes.

The presence of lead and of other cation impurities, intentionally added or unwanted, was detected by the correspond-

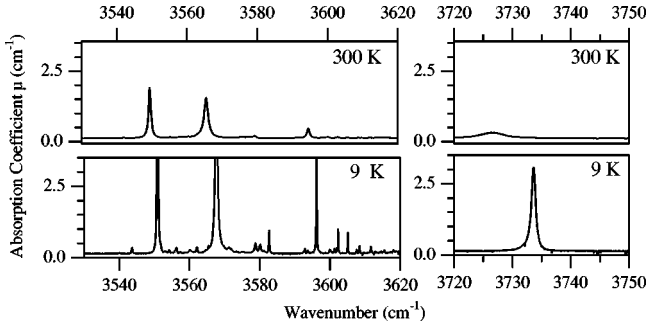

FIG. 5. Role of the temperature in the high-resolution (0.04 cm^{-1}) IR absorption spectra of $KMgF_3$ doped with 0.5% PbF_2 m.f. and grown in air (K21). Spectra measured at 300 K (top) and at 9 K (bottom). Left: spectra in the region of impurity perturbed OH^- stretching modes. Right: line due to the isolated OH^- stretching mode.

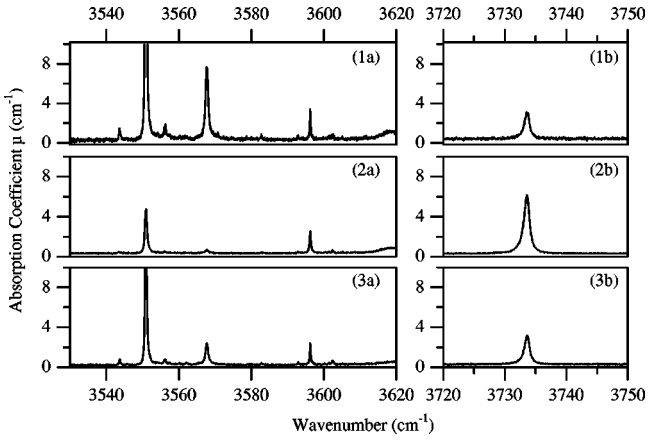

FIG. 6. Role of thermal treatments in the high resolution (0.04 cm^{-1}) IR absorption spectra measured at 9 K of $KMgF_3$ samples doped with 5% $PbBr_2$ m.f. and grown in air (K7). Curves (1): sample as grown and stored at room temperature (RT) for a long time; curves (2): sample quenched from 650 °C to RT; curves (3): sample slowly cooled from 650 °C to RT. Left: spectra in the region of impurity perturbed OH^- stretching modes. Right: line due to the isolated OH^- stretching mode.

ing UV optical absorption bands[17,18,20] (see, as an example, the Pb-related 248 nm peak[20] in Fig. 2). The presence of unwanted impurities in $KMgF_3$ is well known and quoted in the literature.[37] The impurity amount was monitored by the absorption coefficient at the peak of the specific band. In this way, copper, as detected by the broad peak at 310 nm,[18] was found in K0, K4, K14, K21 samples, silver, as detected by the shoulder at ≈210 nm,[17] was found in the K0 and K14 samples, and Pb, as detected by the 248 nm peak,[20] was present not only in the K7, K21, K3, and K4 samples, intentionally Pb doped [see curves (1a)–(3a) in Fig. 1], as expected, but also in the K0 sample, which was intentionally Ag doped [see curve (4a) in Fig. 1].

IV. DISCUSSION

A. Nature of the defects responsible for the IR spectra

The narrow IR lines displayed in Fig. 1 are attributed to OH^- -stretching modes on the basis of the following considerations.

(a) They occur only in samples either doped with KOH [see curves (6a) and (6b) in Fig. 1] or grown in air [see curves (1) to (5)]. In fact, the water molecules, present in the damp atmosphere, dissociate at the temperature of the crystal growth (1050 °C), supplying the OH^- ions which easily enter the lattice, the substitution of OH^- for F^- being favored by the same electrical charge and comparable ionic radius [the OH^- radius is 1.36 Å (Ref. 38) while the F^- Pauling radius is 1.33 Å].

(b) The presence of OH in the lattice is confirmed by the UV band peaking at 187 nm and due to the transition between the electronic ground and first excited states[22] (see Fig. 2).

(c) The wave number range in which the IR lines, their isotopic replicas and overtones occur is typical for the corresponding OH^--stretching modes in alkali halides[23–25,31] (see Table I).

(d) The isotopic shift of most lines, as a consequence of the substitution within the hydroxyl ion either of D for H or of ^{18}O for ^{16}O (see Sec. III and Figs. 3 and 4), is in good agreement with that expected on the basis of the reduced mass ratio of the ^{16}OD or ^{18}OH free molecules to that of the ^{16}OH respectively [see Eq. (1)].

To be more precise, the line displayed in the right side column of Fig. 1 peaks at 3733.7 cm^{-1} at 9 K, i.e., very close to the OH^--stretching mode absorption position in LiF and NaF (see Table I). As for LiF and NaF, the line is present in only OH-doped samples, and thus the 3733.7 cm^{-1} line in $KMgF_3$ is attributed to isolated OH^-, substituting for an F^- at the center of the cubic unit cell face. By assuming for the OH^- vibrational transition in $KMgF_3$ the same oscillator strength as that determined by Guckelsberger for OH^- in LiF,[39] the isolated OH^- concentration in $KMgF_3$ can be estimated as

$$n_{OH}(\text{ppm}) \approx 10 \times \mu_{3733}(\text{cm}^{-1}), \tag{2}$$

where μ_{3733} is the absorption coefficient at 3733.7 cm^{-1}, measured at 9 K. Therefore the isolated OH^- concentration in Pb doped $KMgF_3$ samples, investigated in the present work, is a few tens of ppm. The isolated OH^- concentration is high in samples grown in air and nominally doped with Ag [see curves (4b) and (5b) in Fig. 1], where the Pb concentration is either low or negligible (see also Sec. IV B). It is quite low (≈1.7 ppm) in nominally pure samples grown in inert atmosphere, despite the fact that KOH was added to the melt [see curve (6b) in Fig. 1]. Such a low OH^- doping can be accounted for, since the KOH melting point (≈360 °C) is much lower than the temperature at which the $KMgF_3$ crystal is grown (≈1050 °C): KOH loss might take place due to evaporation.

As already mentioned in Sec. III, the IR lines displayed in the left side column of Fig. 1 are detected in samples codoped with OH and metal cations. A few lines, such as those peaking at 3582.73, 3596.20, and 3603.62, and displayed also in Fig. 1, were recently attributed to the Cu-OH interaction:[35] the unwanted presence of Cu being monitored in the samples by the UV absorption at 310 nm[18] (see Sec. III). In the present work the codoping impurity is Pb, whose presence in the sample is confirmed by the UV band peaking at 248 nm (Ref. 20) (see Fig. 2). Therefore, as for many alkali halides codoped with divalent or trivalent cations,[25,32] the lines are attributed to OH^- stretching modes, perturbed by neighboring defects in which the metal impurity is embedded. The two main lines at 3550.9 and 3567.7 cm^{-1} are easily ascribed to the OH^- stretching mode perturbed by Pb-induced defects; in fact, they appear in all intentionally Pb-doped samples, i.e., K7 [curve (1a) in Fig. 1], K21 [curve (a) in Fig. 3], K3 [curve (2a) in Fig. 1], and K4 [curve (3a) in Fig. 1], and in the K0 [curve (4a) in Fig. 1] sample, intentionally Ag doped, but in which the 248 nm band was also detected, proving an unwanted Pb contamination. Such an

attribution allows even very small Pb traces to be monitored in other nominally Ag-doped samples, such as K14: in fact, in Fig. 4 [curve (2a)] two very weak lines (indicated by a star) are detected at 3550.9 and 3567.7 cm^{-1}. The narrow weak IR lines emerge distinctly from the flat background, revealing the Pb contamination, which escapes detection by means of the broad UV band at 248 nm. In addition to the two main lines, other weaker lines (at least ten) can be attributed to the OH^--stretching modes perturbed by Pb-induced defects, by analyzing the spectra of either heavily Pb-doped and/or thick samples: an example is provided by curve (1a) in Fig. 4, related to a 4 mm thick sample. The positions and widths of a few minor Pb-OH lines are collected in Table I.

The presence of many lines, which are attributed to the Pb-OH interaction, can be accounted for by the variety of Pb-induced defects, in which OH^- is embedded, acting as a very sensitive probe of the surrounding. A model for a simple Pb-OH complex can be envisaged as a Pb^{2+} replacing a K^+ at the corner of the cubic unit cell and neighboring an OH^- which substitutes for an F^- at the center of the cubic unit cell face. The compensation of the positive charge excess, introduced by the $Pb^{2+} \rightarrow K^+$ substitution, might be provided by a K^+ vacancy. The substitution of Pb^{2+} for K^+, rather than for the homovalent Mg^{2+}, is supported by the following considerations.

(a) The lattice mismatch is lower: in fact the Pb^{2+} radius ($\approx$1.2 Å) is close to that of K^+ ($\approx$1.3 Å), but larger than that of Mg^{2+} ($\approx$0.7 Å).

(b) The ODMR (Ref. 21) and polarized luminescence[40] measurements provide a model for the Pb *Z* center in $KMgF_3$ as a Pb^{2+} substituting for a K^+, charge compensated by a K^+ vacancy, near to an *F* center.

The charge compensation of Pb^{2+} might be supplied by the K^+ vacancy either locally or far from the Pb^{2+} ion: in the former case, different coordinations of the Pb^{2+}-K^+-vacancy complex are expected, as for divalent impurity-cation vacancy complexes in alkali halides. Therefore, several configurations of the simple Pb-OH defect, described above, can be envisaged, in part accounting for the rich IR spectrum, displayed, as an example, in Fig. 4 [curve (1a)].

As is well known in other ionic materials (e.g., alkali halides, CaF_2), the impurities, unless present in concentrations below their solubility limit in a given matrix, give rise to clustering and aggregation phenomena.[41] Therefore, OH^- embedded in a variety of Pb clusters can be monitored by additional IR lines. The occurrence of OH within aliovalent metal impurity clusters was recently assumed as being responsible for the complex anelastic relaxation spectra of the rare-earth doped perovskite structured $BaCeO_3$.[30] Suitable thermal treatments (see Secs. II and III) are able to break clusters and/or complexes (e.g., quenching from high temperatures), or can favor the impurity association and clustering (e.g., slow cooling from high temperatures).[41] Their effects on the IR spectrum of a $KMgF_3$:Pb sample are portrayed in Fig. 6. The sample quenching from 650 °C strongly reduces the lines due to OH-Pb interaction (the two main ones peaking at 3550.9 and 3567.7 cm^{-1}), and increases the 3733.7 cm^{-1} line, attributed to the isolated OH^- [compare curves (2a) and (2b) with curves (1a) and (1b), respectively, in Fig. 6]: this means that the dissociation of Pb complexes and/or Pb clusters in which OH^- was embedded supplies simpler Pb defects and isolated OH^- centers. The same result is seen in deuterated samples (see Fig. 3). In fact, in order to perform the substitution of OD for OH, the sample is kept at a still higher temperature [950 °C (see Sec. II)], which further shifts the thermodynamic equilibrium between the Pb-OH^- complexes and the dissociated species, such as OH^- and Pb^{2+}, towards the latter ones. Moreover, the subsequent cooling to room temperature (RT) can be regarded as a fast quenching for the very thin surface layer in which the isotopic substitution was effective, as proved in LiF:Mg:[42] the high-temperature defect distribution remains practically frozen in, as shown by curves (e) and (f) in Fig. 3. In fact, the lines due to the OD^--Pb complexes at 2619.7 and 2630.1 cm^{-1} are very weak [curve (e)], while the line due to isolated OD^- is, in comparison, very strong [curve (f)].

The subsequent annealing from 650 °C of the hydroxylated sample causes the partial recovery of the 3550.9 and 3567.7 cm^{-1} lines and a decrease of the 3733.7 cm^{-1} line [compare curves (3a) and (3b) with curves (1a) and (1b), respectively, in Fig. 6], stressing that the defects responsible for the first two lines are Pb complexes or clusters in which OH^- is included. The presence of Pb clusters in as grown $KMgF_3$ samples is also proved by the UV shoulder at 204 nm (see Fig. 2): this absorption, attributed to Pb dimers, is suppressed as a consequence of the sample quenching.[20] The relative amplitude of the various Pb-OH^- lines may change from sample to sample (see Fig. 1), as a consequence of their differing thermal history.

B. Role played by Pb contamination on the other IR lines

Lead affects considerably the OH-related IR spectra of $KMgF_3$ crystals, as follows.

(a) The presence of lead, as of silver and copper, favors the OH inclusion in $KMgF_3$ crystals grown in air,[33] as shown by UV and IR spectra.

(b) Lead strongly interacts with OH giving rise to a variety Pb-OH complexes and clusters, monitored by the IR lines quoted in Table I and displayed in Fig. 1 by curves (1a)–(4a). The higher the lead content in the sample, as monitored either by the absorption coefficient at 248 nm or by the amplitude of the 3550.9 and 3567.7 cm^{-1} lines [see Fig. 1, curves (1a)–(4a)], the lower the amplitude of the 3733.7 cm^{-1} due to isolated OH^- [see Fig. 1, curves (1b)–(4b)]. Figure 7(f) displays the absorption coefficient at 3733.7 cm^{-1} (for the samples whose absorbance at 3733.7 cm^{-1} was not too high and could be correctly evaluated) vs that at 248 nm. Therefore the Pb-OH^- centers seem to lower more effectively the crystal free energy than does the isolated OH^-.

(c) The presence of lead in the lattice causes the broadening of the lines, mainly due to OH^- interacting with other impurities, e.g., 3582.7 and 3596.2 cm^{-1} lines due to Cu-OH^-, and 3605.1 cm^{-1} due to the OH^- interaction with an unidentified impurity.[35] This effect is summarized by Fig. 7:

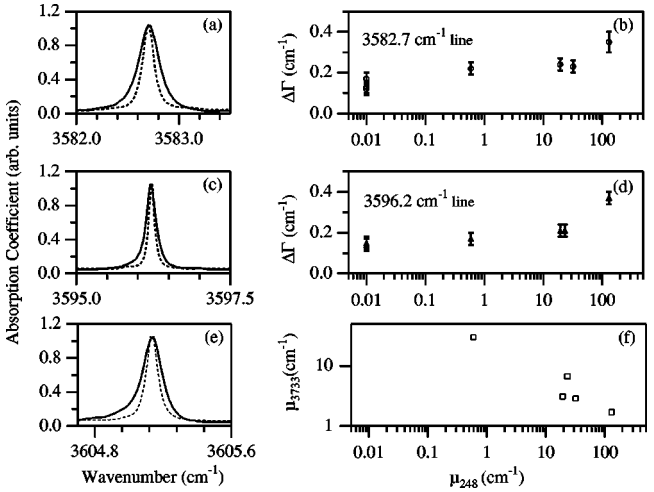

FIG. 7. Effect of the Pb doping on the OH-stretching modes. In (a), (c), and (e) windows the high-resolution (0.04 cm^{-1}) IR absorption spectra measured at 9 K of a $KMgF_3$ sample doped with 0.5% PbF_2 m.f. and grown in air (K21) (solid line) and of a $KMgF_3$ doped with 12.5% AgI m.f. and grown in air (K14) (dashed line) are compared with the 3582.7, 3596.2, and 3605.1 cm^{-1} lines, respectively. For the sake of clarity, the absorption lines are normalized to their maximum amplitude. In (b) and (d) windows the full widths at half maximum $\Delta\Gamma$, measured at 9 K, of the 3582.7 and 3596.2 cm^{-1} lines, respectively, are displayed as a function of the absorption coefficient μ_{248} at the maximum of the UV band peaking at 248 nm, which increases with the Pb concentration. In the (f) window the absorption coefficient at the maximum of the 3733.7 cm^{-1} IR line, due to the isolated OH^- stretching mode, μ_{3733} is plotted vs μ_{248}.

on the left side, the normalized line shapes of the abovementioned lines are portrayed for a Pb doped sample (solid line) and for a nominally ''Pb-free'' one (dashed line) and, on the right, the related line widths are plotted vs the absorption coefficient at 248 nm.

The broadening can be explained by the static disorder induced in the lattice by Pb^{2+} substituting for a K^+ and by the charge compensating K^+ vacancy (inhomogeneous broadening): in fact, the charge distribution is locally altered with respect to that of the perfect lattice, and the induced electric fields slightly modify the OH^--defect stretching frequency.[43] A similar inhomogeneous broadening of the OH^- stretching absorption lines is reported as due, in a BSO sillenite, to P doping,[32] in $KTaO_3$ to Co and Ni doping,[44] and in $LiNbO_3$ to nonstoichiometry.[28] The result stresses once more the sensitivity of the OH^- stretching mode to even slight modifications of the environment, not only those occurring in a Pb complex or Pb cluster (short range effects) and responsible for the variety of IR lines, but also those due to a random distribution of charge excess bearing species, as Pb^{2+} and K^+ vacancy (long range effects).

C. Anharmonicity of OH^- stretching modes

The existence of anharmonic effects is detected by the presence of the overtone lines in the range 6900–7300 cm^{-1}(see Sec. III and Fig. 3) and by the discrepancy, within 2%, between the line position predicted by Eq. (1) in the case of isotopic substitution and the observed value. The model of the anharmonic oscillator in the Morse potential, already successfully used to describe the anharmonicity of the OH^- vibrational modes in insulating crystals,[45] is applied in the present case. The Morse potential U, as a function of the distance r, is

$$U(r-r_e)=D_e\{1-\exp[-\beta(r-r_e)]\}^2, \tag{3}$$

where D_e and β are the Morse potential parameters, D_e is the binding energy and r_e is the equilibrium distance.

The related Schrödinger equation is analytically solved, its eigenvalues $G(n)$ being

$$G(n)=\omega_e\left(n+\frac{1}{2}\right)\left[1-x_e\left(n+\frac{1}{2}\right)\right], \tag{4}$$

where n, ω_e, and x_e are the vibrational quantum number, the oscillator natural frequency and the anharmonicity parameter, respectively. They are related to the Morse potential parameters D_e and β and to the oscillator reduced mass μ as follows:

$$\omega_e=\beta\left(\frac{\hbar D_e}{\pi c\mu}\right)^{1/2}, \tag{5}$$

$$\omega_e x_e=\frac{\hbar\beta^2}{4\pi c\mu}. \tag{6}$$

In the above equations $G(n)$ and ω_e are wave numbers, c is the vacuum light velocity, and $\hbar$ is the reduced Planck constant.

The anharmonicity parameter can be evaluated in different ways.

(i) From the isotopic substitution, as $x_{em}^{\rm is}$:

$$x_{em}^{\rm is}=\frac{1}{2}\times\frac{1-\rho^{1/2}R}{1-\rho R}, \tag{7}$$

where R and ρ are the $\Delta G_{10}^{\rm OH}/\Delta G_{10}^{\rm OD}$ and $\mu_{\rm OD}/\mu_{\rm OH}$ ratios, respectively, $\Delta G_{10}^{\rm OH}$ and $\Delta G_{10}^{\rm OD}$ are the wave numbers of the $0\rightarrow1$ transition for OH and OD, respectively. In the present case ρ is assumed as $\rho_f=0.5300$, i.e., the ρ value for the free diatomic molecule. This is an approximation, since OH is not free but embedded in a lattice: its validity is discussed below.

(ii) From the first overtone ΔG_{20}, as $x_{em}^{\rm ov}$:

$$x_{em}^{\rm ov}=\frac{1}{2}\times\frac{\Delta G_{20}-2\Delta G_{10}}{\Delta G_{20}-3\Delta G_{10}}, \tag{8}$$

where ΔG_{n0} is the wave number of the transition $0\rightarrow n$ transition.

(iii) From the ratio $I_{0\rightarrow2}/I_{0\rightarrow1}$, as x_{ee}:

$$x_{ee}\simeq\frac{I_{0\rightarrow2}}{I_{0\rightarrow1}}, \tag{9}$$

where $I_{0\rightarrow2}$ and $I_{0\rightarrow1}$ are the transition probabilities for the fundamental and the first overtone, respectively.[45] Experi-

TABLE II. Morse parameters for OH^--related defects in $KMgF_3$ evaluated at 9 K and compared with those reported for other matrices or species.

Matrix or species	Impurity	ΔG_{10} cm^{-1}	$x_{em}^{ov}\times 10^2$	$x_{em}^{is}\times 10^2$	$x_{ee}\times 10^2$	D_e eV	$\beta\times 10^{-8}$ cm^{-1}	ρ
$KMgF_3$	Pb	3550.9	2.22	2.34	2.7 ± 0.3	5.18	2.15	0.531
	Pb	3567.7	2.29	2.27	2.6 ± 0.3	5.05	2.19	0.529
	Cu	3582.7	2.20	2.28	4.2 ± 0.6	5.27	2.15	0.530
	Cu	3596.2	2.19	2.24	3.2 ± 0.4	5.31	2.15	0.530
		3733.7	2.13	1.85	0.7 ± 0.1	5.70	2.15	0.528
LiF	Mg	3573.6[a]	2.26	2.41	0.45	5.13	2.18	0.531
		3735.4[b]		1.85	$<10^{-3}$	5.30		
NaF	Mg	3592.5[a]	2.22	2.35	1.9	5.50	2.16	0.531
		3737.4[b]	2.22	1.75	0.2	5.46	2.21	0.527
KF		3722.5[b]	2.22	1.78	2.2	5.43	2.21	0.527
LiBr		3644.8[b]	2.27	2.31	5.9	5.22	2.21	0.530
$BaTiO_3$		3485.5[c]	2.37	2.63		4.79	2.20	0.531
$SrTiO_3$		3495.4[d]	2.37	2.53		4.8	2.21	0.531
$LiNbO_3$		3483[e]	2.56	2.70		4.44	2.29	0.531
		3465.9[f]	2.56	2.67	0.45	4.43	2.28	0.531
free OH^-		3555.6[g]		2.45		4.5	2.27	

[a]From Ref. 32, $T=9$ K.
[b]From Ref. 31, $T=12$ K.
[c]From Ref. 46, $T=300$ K.
[d]From Ref. 47, $T=300$ K.
[e]From Ref. 27, $T=300$ K for congruent samples.
[f]From Ref. 28, $T=293$ K for stoichiometric samples.
[g]From Ref. 36, the equivalent rotational temperature being 1000 K.

mentally x_{ee} is the ratio between the areas subtended under the corresponding absorption lines.

The ρ parameter can be evaluated without any assumption from Eq. (7), if x_{em}^{ov} and R are known from the experimental data, i.e., if for a given OH^- defect, ΔG_{10}^{OH}, ΔG_{10}^{OD}, and ΔG_{20}^{OH} can be measured. The ρ values obtained in this way can be tested against various force-constant models for the defect. The binding energy D_e, β, and ω_e can also be evaluated, if ΔG_{10} and ΔG_{20} are known, by using Eqs. (5), (6), and (8).

β, D_e, x_{em}^{ov}, x_{em}^{is}, x_{ee}, and ρ were determined for a few lines of the $KMgF_3$:Pb spectrum: their values, as measured at 9 K, are collected in Table II and compared with those related to OH^--induced defects in a few alkali halides[31,32] and perovskitic oxides.[27,28,46,47] The temperature dependence of β, D_e, ω_e, x_{em}^{ov} in the range 9–300 K for the 3550.9, 3567.7 (due to OH^--Pb), and 3596.2 cm^{-1} (due to OH^--Cu) lines is displayed in Fig. 8.

The anharmonicity parameter x_{em}^{ov} values for OH^--related defects in $KMgF_3$ are very close to those reported for alkali halides[31,32] and lower than those of perovskitic oxides[27,28,46,47] (see Table II). This suggests a lower anharmonicity of the OH^--stretching mode in $KMgF_3$ and alkali halides compared with the perovskitic oxides, as also confirmed by the higher values of the binding energy D_e and the lower values of β (see Table II). The anharmonicity parameter x_{em}^{ov}, as evaluated from Eq. (8), does not coincide with x_{em}^{is}, as evaluated from Eq. (7), see Table II. In fact, in the former calculation, no assumption is required, while in the latter ρ is assumed as being $\rho_f=0.5300$. If ρ is directly calculated from the experimental data (see above), its value may be different from ρ_f (see last column in Table II) accounting for the difference between x_{em}^{ov} and x_{em}^{is}. Figures of ρ higher than ρ_f were explained by assuming a coupling of the OH^- vibration to the neighboring ions: in fact, a simple model of OH^- strongly coupled to the lattice through oxygen supplies a value of $\rho_c=0.5364$.[45] As shown in Table II, ρ values slightly higher than ρ_f and significantly lower than ρ_c are found for the lines peaking at 3550.9 cm^{-1} (OH^--Pb center) in $KMgF_3$, 3573.6 cm^{-1} in LiF, 3592.5 cm^{-1} in NaF (both OH^--Mg centers), and for all the OH^--related lines in perovskitic oxides quoted in Table II. This means that OH^- behaves as a nearly free diatomic molecule in the above mentioned defects and matrices. In a few cases, mainly in pure fluorides (e.g., $KMgF_3$, LiF, NaF, and KF), ρ is lower than ρ_f: very likely, the cage provided by the ions surrounding OH^- is too tight; in fact, the ionic radius of OH^- is practically the same[38] as that of F^- (see Sec. IV A). As a consequence, the model of OH^- as a free diatomic molecule fails.[32] This restriction does not hold true for OH^-, either substituting for a larger anion such as Br^- in LiBr (see Table II), or perturbed by Mg in LiF and NaF and by Pb in $KMgF_3$ (3550.9 cm^{-1} line): the charge compensating cation vacancy (see Sec. IV A) provides some space where the

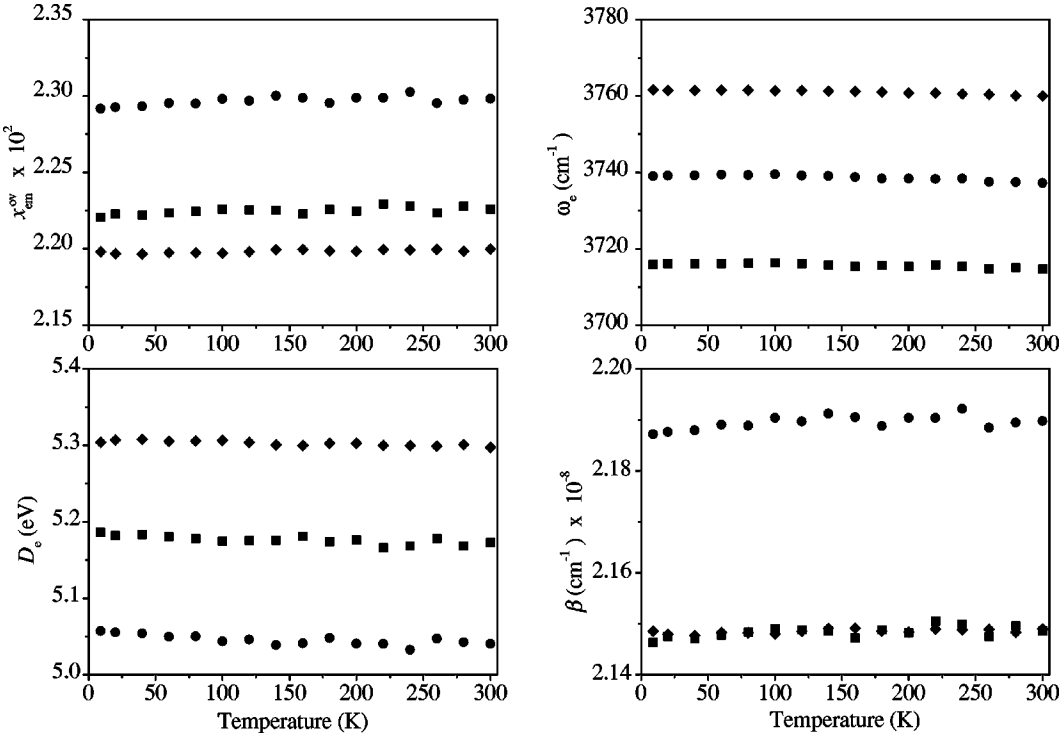

FIG. 8. Temperature dependence of the anharmonicity x_{em}^{ov}, oscillator natural frequency ω_e, and Morse parameters (D_e and β) for OH^- modes monitored by the 3550.9 (squares), 3567.7 (circles), and 3596.2 cm^{-1} (diamonds) lines in the high-resolution (0.04 cm^{-1}) IR absorption spectra of a $KMgF_3$ sample doped with 0.5% PbF_2 m.f. and grown in air (K21).

OH^- can oscillate as nearly free. Also, the ρ value for the Pb-OH^- line peaking at 3567.7 cm^{-1} in $KMgF_3$ is 0.529, i.e., lower than ρ_f: the result can be accounted for by assuming that the charge compensating K^+ vacancy is not a next nearest neighbor of the OH^- in the Pb-OH^- defect, and thus the cage in which OH^- is embedded remains rather tight. For the Cu-OH^- lines peaking at 3596.2 and 3582.7 cm^{-1} ρ equals ρ_f, within the experimental error (see Table II): Cu^+ is smaller than K^+, which it substitutes, providing some space to the neighboring OH^- oscillator (the ionic radii of Cu^+ and of K^+ are 0.96 and 1.33 Å , respectively).

In the framework of the Morse model, if the electric-dipole moment is proportional to the O-H separation, the anharmonicity parameter x_{ee}, as defined by Eq. (9), should equal x_{em}^{ov}: Table II shows that this requirement is not fulfilled for all the OH^--stretching modes in $KMgF_3$, as for a few similar defects in alkali halides and perovskitic oxides.[28,31,32,45] This means that such modes are characterized by electrical anharmonicity, in addition to the mechanical one expressed by x_{em}^{ov}, i.e., the OH dipole moment does not scale linearly with the O-H distance.[45,48,49]

By increasing the temperature the anharmonicity of the Morse potential slightly increases, as shown in Fig. 8 for the Pb-OH^- defects (3550.9 and 3567.7 cm^{-1} line) and a Cu-OH^- center (3596.2 cm^{-1} line). In fact, D_e decreases, while β increases, and, as a consequence, the mechanical anharmonicity x_{em}^{ov} increases. The anharmonicity enhancement can be regarded as a result of the lattice thermal expansion.

D. Phonon-coupling of the OH stretching modes

The analysis of the line position $\Delta G(T)$ and width $\Gamma(T)$, as a function of the temperature T, supplies information on the phonon coupling of the OH^- localized modes. The absorption lines broaden, weaken and shift towards lower wave numbers as the temperature is increased (see Fig. 5). Since the lines detected are, as a rule, very narrow (see Table I), a weak coupling of the OH^--stretching mode to the lattice vibrations is expected; therefore, the line position $\Delta G(T)$ and width $\Gamma(T)$ are analyzed in the framework of the single phonon coupling model,[34] as in the case of the OH^--stretching modes in alkali halides and sillenites.[32] According to the model, the localized mode is coupled to a single phonon band of frequency ω_0 and width γ by a coupling constant $\delta\omega$. In the weak coupling the limit is $|\delta\omega| \ll \gamma$. As a consequence, the IR absorption line is Lorentzian shaped and the temperature dependence is described as

$$\Delta G(T) = \Delta G_0 + \delta\omega \left[\exp\left(\frac{h\omega_0}{KT} \right) - 1 \right]^{-1}, \tag{10}$$

$$\Gamma(T) = \Gamma_0 + \frac{2(\delta\omega)^2}{\gamma} \exp\left(\frac{h\omega_0}{KT} \right) \left[\exp\left(\frac{h\omega_0}{KT} \right) - 1 \right]^{-2}, \tag{11}$$

where ΔG_0 and Γ_0 are $\Delta G(T)$ and $\Gamma(T)$ at $T=0$ K, respectively.

The IR lines due to the OH^- stretching modes are well described by Lorentzian curves, an example being supplied

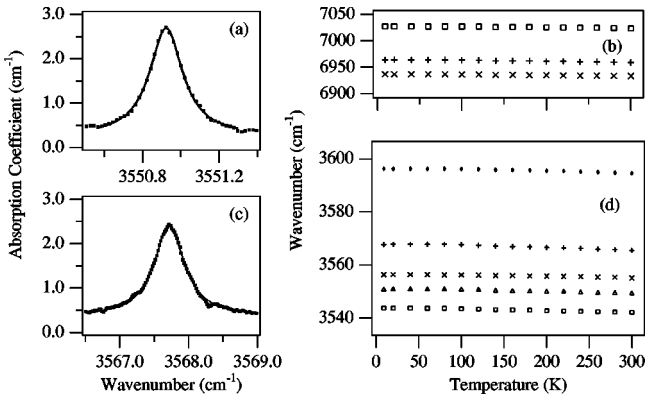

FIG. 9. Line shape and temperature dependence of the line position for OH^- stretching modes perturbed by impurities in $KMgF_3$ samples. Left: line shape of the 3550.9 (top) and 3567.7 cm^{-1} (bottom) lines (both due to Pb-OH stretching modes) in a $KMgF_3$ sample nominally doped with 2.5% AgI and grown in air (K0): the dots are the experimental data, taken at 9 K, while the solid line provides the fitting according to a Lorentzian line shape. Right: temperature dependence of the line position for a number of lines in a $KMgF_3$ sample doped with 0.5% PbF_2 m.f. and grown in air (K21). In the (b) window, starting from the top, the overtones at 7027.1, 6963.7, and 6936.7 cm^{-1} are displayed, while in the (d) window, starting from the top, the fundamentals at 3596.2, 3567.7, 3556.3, 3550.9, and 3543.7 cm^{-1} are portrayed. For the fundamental-overtone correspondence and interacting impurity attribution, see Table I.

by Fig. 9 on the left, for the 3550.9 and 3567.7 cm^{-1} lines. The temperature dependence of the line position is displayed on the right for a few fundamental transitions (bottom), and for their overtones, in the cases in which these could be detected over the entire 9–300 K range (top). The experimental $\Delta G(T)$ values for a few lines fit quite well to Eq. (10) over the 9–300 K range. The fitting of $\Gamma(T)$ according to Eq. (11) could be done for those lines which are not too strong; in fact, in some cases they are either out of scale (see, as an example, Fig. 1) or their amplitude is affected by the nonlinear detector response to weak transmitted light signals. In other cases the lines are too narrow at low temperatures to be correctly resolved on the basis of the available instrumental resolution, which was as good as 0.04 cm^{-1}.

For the 3596.2 and 3733.7 cm^{-1} lines both $\Delta G(T)$ and $\Gamma(T)$ could indeed be fitted simultaneously to Eqs. (10) and (11). The fitting parameters $\delta\omega$, ω_0, and γ, so obtained, are listed in Table III. If γ is evaluated, the requirement $|\delta\omega| \ll \gamma$ is fulfilled (see Table III). The frequencies ω_0 of the phonons coupled to the localized OH^- modes (both fundamental and first overtone transitions) are well within the lattice frequency spectrum of the host matrix, and most of them fall in the range of the highest $KMgF_3$ phonon density of states.[50] In particular, the coupled phonon frequencies related to the Pb-perturbed OH^- stretching mode, monitored by the main lines peaking at 3550.9 and 3567.7 cm^{-1}, are close to LO_1 (193 cm^{-1}) mode frequency. Such a mode has been attributed to the eight K^+ ions at the corners of the cubic unit cell vibrating against the six F^- octahedron:[51] a coupling of this mode to the Pb-perturbed OH^- stretching is in agreement with the model proposed above (see Sec. IV A) of an OH^- substituting for an F^- and a Pb^{2+} substituting for a K^+.

For the lines due to isolated OH^- (3733.7 cm^{-1}) and to OH^- perturbed by Cu (3596.2 cm^{-1}), the temperature dependence of their position $\Delta G(T)$ is practically the same, regardless of the Pb concentration in the sample (i.e., ''Pb-free'' or intentionally doped samples) and of the different widths Γ_0 displayed [see Sec. IV B and Figs. 7(c) and 7(d) for the 3596.2 cm^{-1} line]. The coupled phonons, evaluated according to the above analysis, are the same, within the experimental error. This means that the homogeneous line broadening is biased by the same lattice modes, independently of the static disorder induced by lead, which is, however, responsible for the inhomogeneous line broadening.

V. CONCLUSIONS

By monitoring the rich narrow line IR spectrum of $KMgF_3$ samples, doped with varying amounts of lead and submitted to proper thermal treatments and isotopic substitutions, it was possible: (a) to identify the lines due to Pb-perturbed OH^- stretching modes; (b) to provide a model for

TABLE III. Fitting parameters of the position- and width-temperature dependence according to Eqs. (10) and (11) for a few OH^--stretching lines in a $KMgF_3$:Pb sample (K21). $\Delta n = 1, 2$ are related to the fundamental and overtone transitions wave numbers, i.e., ΔG_{10} and ΔG_{20}, respectively, listed in Table I.

Interacting impurity	Δn	ΔG_0 (cm^{-1})	Γ_0 (cm^{-1})	ω_0 (cm^{-1})	$\lvert\delta\omega\rvert$ (cm^{-1})	γ (cm^{-1})
Pb	1	3543.72±0.03		124.10±19.444	1.38±0.28	
	1	3550.96±0.05		181.92±38.47	2.20±0.70	
	1	3556.31±0.02		212.05±26.97	2.05±0.43	
	1	3567.74±0.04		192.42±22.79	3.41±0.62	
Cu	1	3596.23±0.02	0.21±0.01	255.80±17.94	3.96±0.49	24.72±0.94
	1	3733.67±0.11	0.86±0.07	125.80±16.77	5.80±1.01	47.40±1.96
Pb	2	6936.74±0.06	0.61±0.04	140.13±20.30	3.28±0.65	26.89±1.43
	2	6964.00±0.10	1.02±0.05	129.75±23.98	4.13±1.01	36.33±1.59
	2	7027.17±0.05	0.95±0.03	227.65±21.83	6.70±1.07	27.16±4.29

the defects responsible for the lines; (c) to recognize a key role played by lead both in favoring the OH^- inclusion into the matrix and in causing an inhomogeneous broadening mainly of the lines related to OH^- perturbed by different impurities.

The superior sensitivity and selectivity of the high resolution FTIR spectroscopy applied at 9 K was able (a) to discriminate among slightly different environments in which OH^- is embedded, as monitored by the IR narrow lines, at variance with the broad UV band peaking at 187 nm, which accounts for all kinds of OH^--centers; (b) to detect very weak traces of OH^-defects, as in the case of the isotopic replicas due to the ^{18}O present in natural abundance as low as 2×10^{-3} and of the accidental low level Pb doping.

Anharmonicity of the Pb-perturbed OH^- stretching modes, as detected by the weak overtones, was analyzed in the framework of the Morse model: the anharmonicity parameters, binding energies and β values were found to be closer to those reported for alkali fluorides doped with divalent impurities than to those of the perovskitic oxides, revealing the more important role of the ionic character than of the crystalline structure.

The temperature dependence of the line position and linewidth could be well fitted to the single phonon coupling model, as expected for very narrow lines. Most of the phonon frequencies, evaluated in this way, fall in the range of the highest phonon state density of $KMgF_3$, and some of them can be associated to the vibration of K^+ ions against the F^+ ions.

ACKNOWLEDGMENTS

The authors wish to thank C. Sanipoli of the University ''La Sapienza,'' Rome, C. Mora of the GNSM-CNR Unit at the University of Parma, M. Curti of MASPEC-CNR Institute in Parma for technical help, and Professor U. M. Grassano of the University ''Tor Vergata,'' Rome for helpful discussions.

*Present address: Department of Physics, University of Pisa, Via F. Buonarroti 2, 56100 Pisa, Italy.

[1] H. Manaam, Y. Guyot, and R. Moncorge, Phys. Rev. B **48**, 3633 (1993).
[2] G. Hörsch and J. P. Paus, Opt. Commun. **60**, 69 (1986).
[3] A. V. Getkin, V. K. Komar, N. V. Shiran, V. V. Shlykhturov, N. P. Nesterenko, I. M. Krasovitskaya, and V. V. Kornienko, IEEE Trans. Nucl. Sci. **42**, 311 (1995).
[4] C. Furetta, C. Bacci, B. Rispoli, C. Manipoli, and A. Scacco, Radiat. Prot. Dosim. **33**, 107 (1990).
[5] A. F. Buzulutskov, L. K. Turchanovich, and V. G. Vasil'chenko, Nucl. Instrum. Methods Phys. Res. A **292**, 546 (1993).
[6] I. A. Kamenskikh, M. A. MacDonald, V. N. Makhov, V. V. Mikhailin, I. H. Munro, and M. A. Terekhin, Nucl. Instrum. Methods Phys. Res. A **348**, 542 (1994).
[7] P. Dorembos, R. Visser, C. W. E. van Ejik, J. Valbis, and N. M. Khaidukov, IEEE Trans. Nucl. Sci. **42**, 311 (1995).
[8] J. C. Gacon, A. Gros, H. Bill, and J. P. Wicky, Phys. Chem. Solids **42**, 587 (1981).
[9] R. Francini, U. M. Grassano, L. Landi, A. Scacco, M. D'Elena, M. Nikl, N. Cechova, and N. Zema, Phys. Rev. B **56**, 15 109 (1997).
[10] N. Kristianpoller and B. Trieman, J. Lumin. **24-25**, 285 (1981).
[11] S. López-Moraza, J. L. Pascual, and Z. Barandiarán, J. Chem. Phys. **103**, 2117 (1995).
[12] D. R. Lee, T. P. J. Han, and B. Henderson, Radiat. Eff. Defects Solids **136**, 51 (1995).
[13] M. C. Marco de Lucas, F. Rodríguez, and M. Moreno, J. Phys.: Condens. Matter **7**, 7535 (1995).
[14] M. T. Barriuso, J. A. Aramburu, and M. Moreno, J. Phys.: Condens. Matter **11**, L525 (1999).
[15] Y. Wan-Lun and C. Rudowicz, Phys. Rev. B **45**, 9736 (1992).
[16] E. Zorita, P. J. Alonso, R. Alcalá, J. M. Spaeth, and H. Soethe, Solid State Commun. **66**, 773 (1988).
[17] A. Scacco, M. Finocchi, C. Mattei, U. M. Grassano, R. Francini, A. Fardelli, N. Zema, L. Bosi, D. Gallo, M. Martini, and F. Meinardi, J. Phys.: Condens. Matter **9**, 5265 (1997).
[18] T. Tsuboi and A. Scacco, J. Phys.: Condens. Matter **11**, 2787 (1998).
[19] A. Scacco, S. Fioravanti, M. Missori, U. M. Grassano, A. Luci, M. Palummo, E. Giovenale, and N. Zema, Phys. Chem. Solids **54**, 1035 (1993).
[20] M. Missori and A. Scacco, Solid State Commun. **76**, 5 (1990).
[21] J.-M. Spaeth and F. Lohse, Phys. Chem. Solids **51**, 861 (1990).
[22] S. Fioravanti, U. M. Grassano, C. Mattei, A. Scacco, and N. Zema, in *Defects in Insulating Materials*, edited by O. Kanert and J.-M. Spaeth (World Scientific, Singapore, 1993), Vol. 1, p. 574.
[23] F. Lüty, J. Phys. (Paris) **28**, C4-120 (1967).
[24] B. Wedding and M. V. Klein, Phys. Rev. **177**, 1274 (1969).
[25] R. Capelletti, P. Beneventi, E. Colombi, and W. B. Fowler, Nuovo Cimento D **15**, 415 (1993).
[26] M. Stavola, L. Isganitis, and M. Sceats, J. Chem. Phys. **74**, 4228 (1981).
[27] A. Förster, S. Kapphan, and M. Wöhlecke, Phys. Status Solidi B **143**, 755 (1987).
[28] A. Gröne and S. Kapphan, J. Phys. Chem. Solids **56**, 687 (1995).
[29] H. Vormann, G. Weber, S. Kapphan, and E. Krätzig, Solid State Commun. **40**, 543 (1981).
[30] Y. Du and A. S. Nowick, J. Phys. III **6**, C8-637 (1996).
[31] A. Afanasiev and C. P. Lüty, in *Defects in Insulating Materials*, edited by O. Kanert and J.-M. Spaeth (World Scientific, Singapore, 1993), Vol. 1, p. 551.
[32] R. Capelletti, P. Beneventi, and A. Ruffini, Ber. Bunsenges. Phys. Chem. **101**, 1265 (1997).
[33] P. Beneventi, P. Bertoli, R. Capelletti, R. Francini, U. M. Grassano, A. Ruffini, and A. Scacco, Mater. Sci. Forum **239-241**, 449 (1997).
[34] P. Dumas, Y. J. Chabal, and G. S. Higashi, Phys. Rev. Lett. **65**, 1124 (1990).
[35] R. Capelletti, A. Baraldi, P. Bertoli, M. Cornelli, U. M. Grassano, A. Ruffini, and A. Scacco, in *Proceedings of the NATO Advanced Research Workshop on Defects and Surface-Induced Effects in Advanced Perovskites, Jurmala, Latvia, 1999*, edited by G. Borstel, A. Krumins, and D. Millers (Kluwer Academic Pub-

lishers, Amsterdam, 2000), p. 293.
[36] N. H. Rosenbaum, J. C. Owrutsky, L. M. Tack, and R. J. Saykally, J. Chem. Phys. **84**, 5308 (1986).
[37] C. R. Riley and W. A. Sibley, Phys. Rev. B **1**, 2789 (1970).
[38] H. Paus and F. Lüty, Phys. Status Solidi **12**, 341 (1965).
[39] K. Guckelsberger, J. Phys. Chem. Solids **41**, 1209 (1980).
[40] G. Hörsch and J. P. Paus in *International Conference on Defects in Insulating Crystals*, Parma, Italy, 1988 (Centro Grafico dell'Università, Parma, 1988), p. 233.
[41] R. Capelletti, Radiat. Eff. **74**, 119 (1983).
[42] R. Capelletti, P. Beneventi, E. Colombi, and S. Prato, Nuovo Cimento D **20**, 859 (1998).
[43] K. Hermansson, Chem. Phys. **170**, 177 (1993).
[44] S. Jandl, J. Rousseau, and L. A. Boatner, Solid State Commun. **87**, 63 (1993).
[45] W. B. Fowler, R. Capelletti, and E. Colombi, Phys. Rev. B **44**, 2961 (1991).
[46] S. Kapphan and G. Weber, Ferroelectrics **37**, 673 (1981); K. Buse, S. Breer, K. Peithmann, S. Kapphan, M. Gao, and E. Krätzig, Phys. Rev. B **56**, 1225 (1997).
[47] G. Weber, S. Kapphan, and M. Wöhlecke, Phys. Rev. B **34**, 8406 (1986).
[48] M. L. Sage, Chem. Phys. **35**, 375 (1978).
[49] A. R. Woll and W. B. Fowler, Phys. Rev. B **48**, 16 788 (1993).
[50] S. Salaün, M. Mortier, J. Y. Gesland, M. Rousseau, and B. Hennion, J. Phys.: Condens. Matter **5**, 7615 (1993).
[51] C. H. Perry and E. F. Young, J. Appl. Phys. **38**, 4616 (1967).